Supporting Information for

A system for the high-throughput measurement of the shear modulus distribution of human red blood cells

Amir Saadat,[1†] Diego A. Huyke,[2†] Diego I. Oyarzun,[2†] Paulina V. Escobar,[4] Ingrid H. Øvreeide,[5] Eric S.G. Shaqfeh,[1,2,3*] and Juan G. Santiago[2*]

[1]Department of Chemical Engineering, [2]Department of Mechanical Engineering, [3]Institute of Computational and Mathematical Engineering Stanford University, Stanford, CA 94305, [4]Department of Mechanical Engineering, Pontificia Universidad Católica de Chile, [5]Department of Physics, Norwegian University of Science and Technology

[†]AS, DAH, and DIO contributed equally to this work

*Corresponding authors: juan.santiago@stanford.edu, esgs@stanford.edu

In this document, we provide the following complementary results: a detailed description of the computational model; the sensitivity analysis of the shear modulus and other shape parameters; experimental setup details; measurements of shear modulus for several healthy donors; comparison of the shear modulus with literature; correlation of shear moduli and cell speed; and a list of movies that describe the automatic image analysis as well as the impact of orientation and location on the simulation results.

Contents

S.1 Detailed description of the computational model

S.1.1. Governing equations. We here solve the evolution of a single RBC suspended in an incompressible fluid. The conservation of momentum and the continuity is satisfied in both the fluid and membrane sub-domains using the following governing equations:

$$\begin{aligned} \rho \frac{\mathrm{D}\mathbf{v}}{\mathrm{D}t} &= \nabla \cdot \boldsymbol{\sigma}^f \quad \mathbf{x} \in \Omega^f, \\ \rho \frac{\mathrm{D}\mathbf{v}}{\mathrm{D}t} &= \nabla \cdot \boldsymbol{\sigma}^m \quad \mathbf{x} \in \Omega^m, \\ \nabla \cdot \mathbf{v} &= 0 \quad \in \Omega. \end{aligned} \tag{S1}$$

Here, Ω is the total domain which can be broken into two sub-domains corresponding to the volume of the fluid and an infinitely thin suspended RBC membrane Ω^f and Ω^m, respectively. The stress in the membrane and fluid domains are denoted by $\boldsymbol{\sigma}^m$ and $\boldsymbol{\sigma}^f$, respectively. The stress balance is satisfied at the boundary of contact between the membrane and the liquid,

$$(\boldsymbol{\sigma}^m - \boldsymbol{\sigma}^f) \cdot \mathbf{n} = 0 \quad \mathbf{x} \in \Omega^m, \tag{S2}$$

where, $\mathbf{n}$ is an outwardly-pointing unit normal vector. The suspending fluid is Newtonian and therefore,

$$\boldsymbol{\sigma}^f = \boldsymbol{\sigma}^N = -p\mathbf{I} + \eta\left(\frac{\partial \mathbf{v}}{\partial \mathbf{x}} + \frac{\partial \mathbf{v}^{\mathrm{T}}}{\partial \mathbf{x}}\right). \tag{S3}$$

with, p being the hydrodynamic pressure and η being the Newtonian fluid viscosity. The RBC will be modeled as a 2D hyper-elastic membrane. The stress in the membrane is calculated using the first Piola-Kirchhoff tension,[1] which is related to the second Piola-Kirchhoff tension,

$$\hat{\mathbf{S}} = 2\frac{\partial \widehat{W}}{\partial \hat{\mathbf{C}}} = 2\left\{\frac{\partial \widehat{W}}{\partial I_1^{\hat{C}}}\mathbf{I} + J^2\hat{\mathbf{C}}^{-1}\frac{\partial \widehat{W}}{\partial I_2^{\hat{C}}}\right\}. \tag{S4}$$

In this equation, $\hat{\mathbf{S}}$ is related to the strain energy areal density $\widehat{W}$ using the principle of virtual work. The energy density is a function of the two independent invariants of the right Cauchy-Green tensor $\hat{\mathbf{C}} = \hat{\mathbf{F}}^{\mathrm{T}}\hat{\mathbf{F}}$, i.e., $I_1^{\hat{C}}$ and $I_2^{\hat{C}}$. (Note the caret is used to distinguish 2D tensions the 3D stress counterparts.) The Skalak model [2] is used for the energy areal density of RBC membrane:

$$\widehat{W} = \frac{\mu_s}{2}\left(\frac{1}{2}I_1^2 + I_1 - I_2\right) + \frac{\mu_d}{8}I_2^2. \tag{S5}$$

where $I_1 = I_1^{\hat{C}} - 2$ and $I_2 = I_2^{\hat{C}} - 1$ are the two invariants of the Skalak model. The membrane of the RBC is known to be locally area-incompressible, and this is incorporated in the Skalak model by using a sufficiently larger area dilutional modulus μ_d relative to the shear modulus, μ_s.[2–5]

By assuming RBC as an infinitely thin sack of fluid, we have neglected the out of plane forces in the membrane. Therefore, we need to include an additional energy density function for bending into our RBC model:

$$\widehat{W}_b = \frac{k_b}{2}(2\kappa_H + c_0)^2, \tag{S6}$$

where, k_b is the bending modulus, c_0 is the spontaneous curvature of the membrane, and κ_H is the mean curvature of the membrane. We utilized an immersed-finite-element method (IFEM) to solve the governing equations and simulate the dynamics of coupled fluid-solid problem. The cells start

from an unstressed biconcave shape which also defines the spontaneous shape for bending calculations.[4,6,7] We don't expect the stress-free condition to affect our final results since 1) we use physiological value for the viscosity ratio of cytoplasm to the exterior environment, where the biconcave and a nearly spherical stress-free states found to not show any significant difference.[8,9] More details about our method can be found in our publication.[1]

In this study, we seek to solve the flow field in a constriction geometry with the geometrical details that are depicted in Fig. S1.

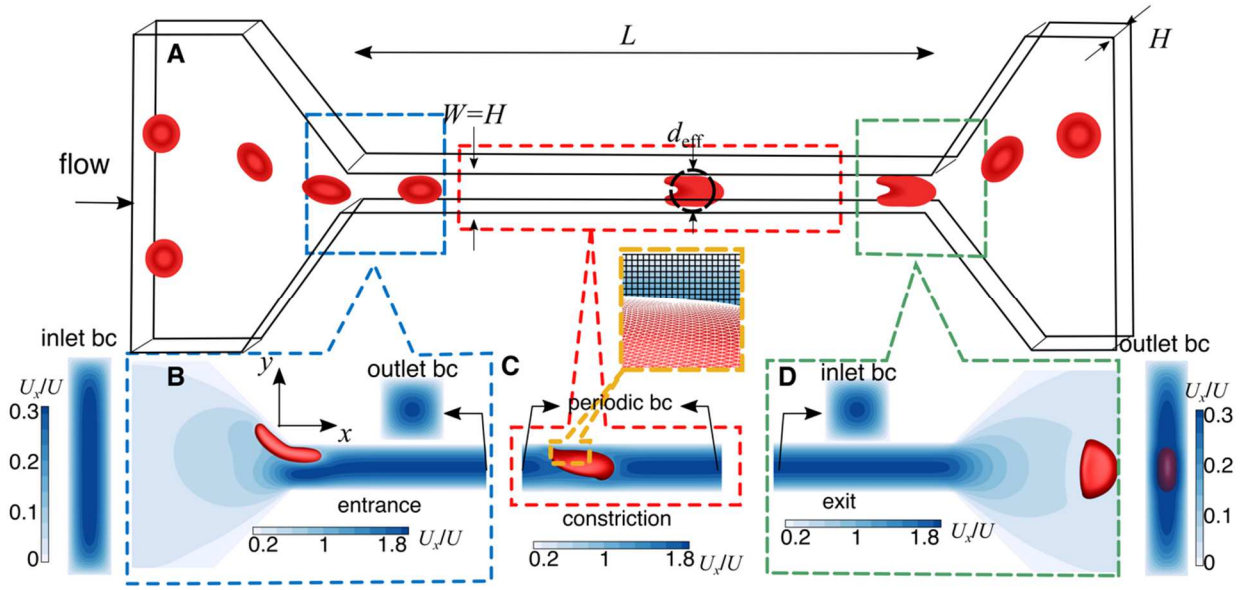

Fig. S1. (A) Schematic representation of the constriction area in the microfluidic platform and the corresponding geometrical parameters. (B)-(D) Computational domain associated with flow simulations behind the surface plot of Fig. 5. Panels (B) and (D) are the simulation domains that are used for evaluating the impact of the initial condition and studying the relaxation dynamics, respectively. Panel (C) shows the simulation domain for finding the steady-state values of *Ta*. Shown in B and D are axial velocity contours (normalized by bulk velocity in the channel) and instantaneous RBC shapes.

S.1.2 Meshing details: Mesh convergence tests for our numerical method have been extensively performed for our previous publications.[1] Here, we use a 4 times greater refined mesh for both RBCs and also the main domain, i.e., 10,242 mesh nodes for each membrane, about 40 Eulerian mesh points across the cell, which leaves us about 10 mesh points across each small clearance "film" between the cells and the wall.

To obtain the important dimensionless parameters that determine the physics of this problem, we nondimensionalized the governing equations. The height of the channel H is considered as the characteristic length, and the unperturbed average velocity of the fluid U as the

characteristic velocity. As a result, U/H is the characteristic time, $\eta\, U/H$ is the characteristic stress in the fluid, and μ_s/H is the characteristic stress in the membrane. This gives us the following non-dimensional equations to solve (non-dimensional variables and operators are indicated with a star):

$$\begin{aligned} &Re\frac{\mathrm{D}\mathbf{v}^*}{\mathrm{D}t^*} = \nabla^*\cdot\boldsymbol{\sigma}^{f*} = -\nabla^* p^* + \nabla^*\cdot\Lambda\nabla^*\mathbf{v}^* \quad x\in\Omega^{\mathrm{f}},\\ &Re\frac{\mathrm{D}\mathbf{v}^*}{\mathrm{D}t^*} = \frac{1}{Ca}\nabla^*\cdot\boldsymbol{\sigma}^{\mathrm{m}*} \quad x\in\Omega^{\mathrm{m}},\\ &\nabla^*\cdot\mathbf{v}^* = 0 \quad x\in\Omega. \end{aligned} \tag{S7}$$

Here Λ is used to account for variable viscosity inside the cytoplasm (within the membrane) η_{cell}. It is defined based on an indicator function Θ which has a value of unity inside the RBC membrane and zero outside and Θ smoothly varies across the boundary.[1,10,11] In particular, $\Lambda = 1 + (\lambda - 1)\Theta$, with $\lambda = \frac{\eta_{cell}}{\eta}$. It is known that the physiological value of the viscosity ratio is significantly greater than unity, in particular, we chose $\lambda = 5$. Additionally, non-dimensional relationships for the energy areal density for the Skalak model and also the bending energy as follows:

$$\begin{aligned} &\widehat{W}^* = \frac{1}{2}\left(\frac{1}{2}I_1^2 + I_1 - I_2\right) + \frac{\mu_d}{8\mu_p}I_2^2,\\ &\widehat{W}_b^* = \frac{\widehat{\kappa}_b}{2}(2\kappa_H^* + c_0^*)^2. \end{aligned} \tag{S8}$$

Overall, 5 dimensionless parameters appear in the governing equations, namely, the Reynolds number ($Re = \rho UH/\eta$), the cytoplasmic viscosity ratio ($\lambda = \eta_{cell}/\eta$), the capillary number ($Ca = \eta U/\mu_s$), μ_d/μ_s, and $\kappa_b = \frac{\mathrm{k}_b}{H\mu_s}$. The value of $\kappa_b = 0.0033$ was chosen in our simulations according to the commonly reported elastic moduli[4,12] and the dimension of our channel, i.e., $k_b \sim 10\times10^{-19}$ N. m and the shear modulus 7×10^{-6} N $^{-1}$.

The literature about the importance of the viscosity of the membrane is controversial. While many researchers neglect the viscosity ratio based on the scaling analysis,[12] some others include it in the simulations[13,14] in the context of a model which contains several other adjusting parameters.

Kelvin-Voigt formula[14] is sometimes used to model the continuum level description of the membrane viscosity as:

$$T_s = \frac{\mu_s}{2}(e^2 - e^2) + 2\eta_m\frac{\partial \ln e}{\partial t}, \tag{S9}$$

where T_s is the maximum shear tension, e is the extension ratio and η_m is the membrane viscosity. The exact range of the viscosity ratio depends on the measurement approach, but more recent diffusion experiments[15] reported the upper bound of η_m as 5×10^{-3} μN. s/m, taking this value, the dissipation across the length of the cell is small, as the Boussinesq number ($Bo = \frac{\eta_m}{\eta_{cell}a}$) is lower than unity.

S.1.3 Derivation of the Taylor deformation. We seek to find the three terms of the moment of area tensor (or the second moment) of the cell image projected into the *xy*-plane, $M_x, M_y, and\ M_{xy}$ following a similar approach described in Chaudhuri and Samanta.[16] Cell region is denoted by Ω.The overall number of points that is used is *N*.

Center of mass coordinates are calculated as, $x_{com} = \frac{\sum_{n\in\Omega} X}{N}$; $y_{com} = \frac{\sum_{n\in\Omega} Y}{N}$. The three main components of the moment of area tensor are,

$$M_x = M_0 = \sum_{n\in\Omega}(X - X_{com})^2, \tag{S10}$$

$$M_y = M_{\frac{\pi}{2}} = \sum_{n\in\Omega}(Y - Y_{com})^2, \tag{S11}$$

$$M_{xy} = \sum_{n\in\Omega}(X - X_{com})(Y - Y_{com}). \tag{S12}$$

The orientation of the object can be determined by minimizing the moment of area around an axis which makes an angle θ with the x axis. The resulting angle can be shown to have the form of Equation (S12). The moment of area at that angle can be obtained based on the relationship between the coordinate values in the rotated frame:

$$\theta = \frac{1}{2}\tan^{-1}\left(\frac{2M_{xy}}{M_x - M_y}\right), \tag{S13}$$

$$M_{x'} = M_\theta = M_x * \cos^2\theta - 2M_{xy}\sin\theta\cos\theta + M_y\sin^2\theta. \tag{S14}$$

Finally, we find the minor and major axes ($2b$ and $2a$, respectively) of an equivalent ellipse which has the same moment of area as the object. Since the moment of area of an ellipse is $M_{y,ell} = \frac{1}{4}\pi a^3 b = \frac{1}{4}ma^2$ and noting that $M_{y'} = M_{\theta+\pi/2}$, we can write

$$a = 2\sqrt{\frac{M_{y,ell}}{I_{tot}}} = 2\sqrt{\frac{M_{y'}}{N}}, \tag{S15}$$

$$b = 2\sqrt{\frac{M_{x,ell}}{I_{tot}}} = 2\sqrt{\frac{M_{x'}}{N}}. \tag{S16}$$

Taylor deformation is then defined as: $Ta = (a - b)/(a + b)$ and is shown in Fig. 2A. Other approaches such as finding the eigen values of the correlation matrix[17] result in the same value of Ta.

S.2 Shear modulus sensitivity versus other shape parameters

S.2.1 Circularity. Here, we show the circularity (also called "form factor")[18] parameter, denoted by *C*, which is determined based on the projected area and perimeter of the cell.[19] The results of *C* as a function of *Ca* clearly demonstrates that the *Ta* has higher sensitivity to *Ca*. In particular, the

steady-state values of *Ca* 0.3 and 0.4 are not distinguishable.

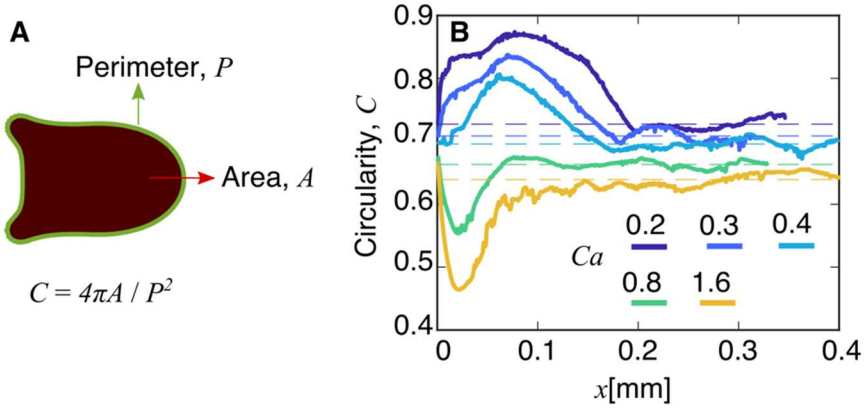

Fig. S2. (A) Definition of circularity based on the projected area and perimeter. (B) Circularity as a function of the position along the constriction. This plot of part B can be contrasted to plot of *Ta* for similar conditions shown in Fig. 2B of the main text. The comparison clearly shows that the *Ta* is a more sensitive shape parameter than circularity and should be used for higher sensitivity shape characterization of red blood cells.

S.2.2 Circular harmonics. The spherical harmonics is a powerful polynomial expansion technique to describe complicated shapes in 3D. [20] We explored the use of circular harmonics to accomplish the same goal in 2D. Similar to the spherical harmonics, associated Legendre polynomial Y_l^m is used, but with no dependency on the azimuthal angle or ϕ , i.e., $m = 0$. In particular, we use the function $r = r_0 + \sum_{l=1}^{n} c_l Y_l^0$, where r is the position of the cell nodal points in polar coordinates, r_0 and c_i are constant coefficients.

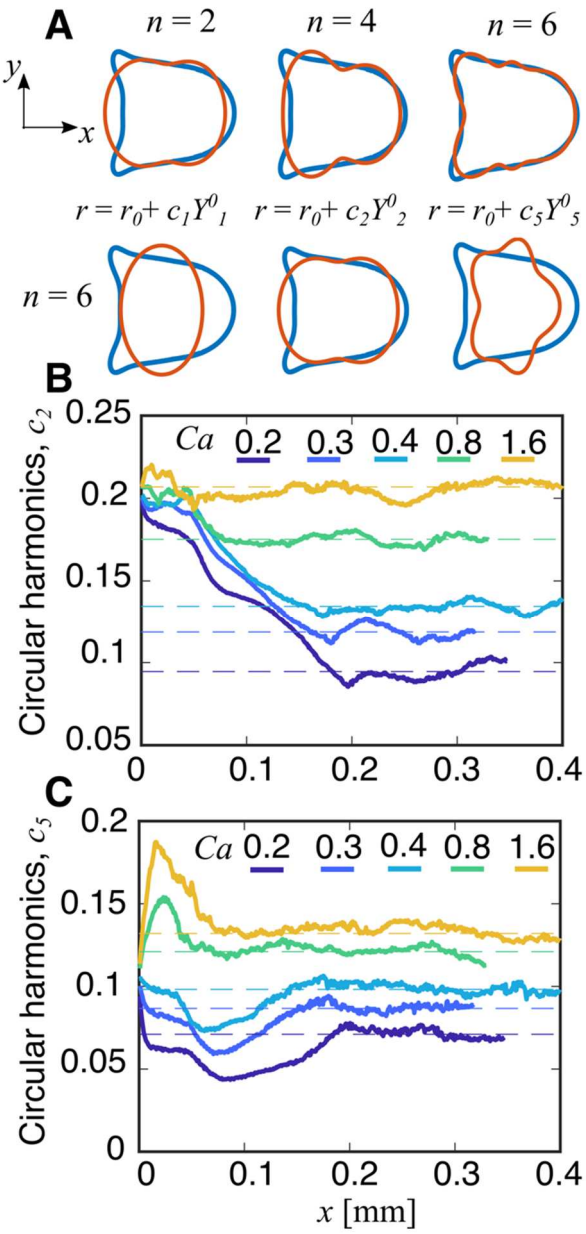

Fig. S3. (A) Top row: Approximation of the shape of the projected cell outline with increasing number of terms in the circular harmonics. Bottom row: Shapes corresponding to various coefficients for the case of $n = 6$ terms in the polynomial. (B), (C) The evolution of the circular harmonics coefficients c_2 and c_5 as a function of x along the constriction, respectively.

Depending on the number of terms in the Legendre polynomial, one can describe the outline of the cells precisely. For instance, in Fig. S3A, we are showing the same outline of the cell, but fitted with different number of terms in the circular harmonics function. We can see that using six terms can very accurately describe the outline. In addition, we demonstrate the shape associated with each one of the coefficients, for instance, the second harmonic coefficient shows the elongation of the cell along the x-axis. It is not then surprising that the second harmonic

coefficient be related to the *Ta* and show sensitivity to the *Ca* as is shown in Fig. S3B.

S.2.3 Shape recovery at exit. We also explored the sensitivity of the cell recovery dynamics to *Ca* in the exit region after the constriction. Fig. S1A shows the domain that we used for this aim and is basically the mirror of the entrance region, except the flow is from the smaller channel (the constriction) to the larger region. The streamlines of the flow around the cell is also shown. We specifically analyzed at the parameter deformation ratio $DR = L_c/W_c$, where L_c and W_c are the values of the bounding box in x and y dimensions, respectively, as the cells recover to their undeformed state.[14]

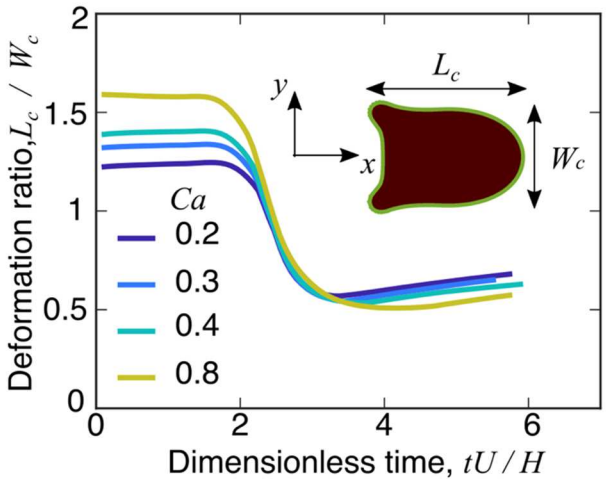

Fig. S4. Deformation ratio, as defined based on the inset figure, is shown as a function of the dimensionless time for the cells that flow in the exit region (see Fig. S1D). The curves associated with different *Ca* clearly shows that the deformation values are more distinguishable within the constriction compared to the relaxation dynamics, i.e., the drop of the deformation and the recovered values after about two dimensionless times.

Fig. S4 shows deformation ratio *DR* as a function of the dimensionless time $\underline{tU/H}$. One can clearly distinguish the curve in the initial part of the simulation during the cell travel inside the constriction for dimensionless time less than about 2. The relaxation dynamics, i.e. the drop of *DR* and the final values of *DR* exhibit weaker dependence on capillary number values.

In Table S1, we summarize the numerical values of the variables, the confinement level, ϵ, the Taylor deformation, *Ta*, the normalized velocity of the cells (U_{cell}/U that was used to construct the surface plot in Fig. 3B and also Fig. 2F.). Commonly, the deformation index ($DI = L_c - W_c/L_c + W_c$, where L_c and W_c are the values of the bounding box in x and y dimensions, respectively) is used to characterize the shape of RBCs. Our analysis suggests that deformation index or deformation ratio, although more sensitive than circularity, still demonstrate fluctuating behavior downstream of the constriction and more dependency on the small changes in the

membrane shape and therefore are more sensitive to the initial condition. Therefore, using *Ta* is preferred as a more reliable shape parameter. Nevertheless, we report the values of *DI* in Table S1.

Table S1. ϵ, Ta, $\frac{U_{cell}}{U}$, and DI values for different isocapillary lines that is used for making the surface plot, in Fig. 3B and also Fig. 2F of the main work. Note that deformation index (*DI*) is related to deformation ratio (*DR*) using $DI = (DR - 1)/(DR + 1)$.

Ca	ϵ	Ta	U_{cell}/U	DR	DI
0.2	0.893, 1.01	0.0715, 0.1392	1.228, 1.119	1.224, 1.438	0.101, 0.18
0.3	0.783, 0.897, 1.011, 1.137, 1.280	0.029, 0.113, 0.173, 0.227, 0.283	1.371, 1.272, 1.165, 1.052, 0.898	1.096, 1.313, 1.526, 1.763, 2.06	0.046 0.135 0.208 0.276 0.347
0.4	0.785, 0.9, 1.023, 1.147, 1.29	0.069, 0.141, 0.206, 0.259, 0.31	1.397, 1.3, 1.202, 1.088, 0.934	1.190, 1.385, 1.63, 1.851, 2.123	0.087, 0.161, 0.239, 0.298, 0.36
0.8	0.781, 0.907, 1.036, 1.166 1.317	0.133, 0.208, 0.264, 0.316, 0.368	1.449, 1.363, 1.265, 1.154, 1.007	1.381, 1.567, 1.787, 2.027, 2.323	0.149, 0.221, 0.282, 0.339, 0.399
1.6	0.785, 0.916, 1.046, 1.176, 1.332	0.217, 0.27, 0.316, 0.358, 0.406	1.5, 1.416, 1.315, 1.205, 1.057	1.629, 1.767, 1.945, 2.18, 2.466	0.239, 0.277, 0.321, 0.371, 0.423

S.3 Shear modulus sensitivity analysis

S.3.1 Viscosity ratio effect on the transient behavior. The viscosity ratio is not exactly known and is usually approximated based on the Hb concentration. In the literature [21,22], values in the range of 3-10 have been considered with most using 5 for the physiological situation [23], and therefore we chose 5. We determined the sensitivity of the results due to increasing the ratio to 10. As is depicted in Fig. S5 below, we found that changing the viscosity ratio to 10 affects the transient evolution, while marginally changes the steady-state values of the Taylor deformation, confinement, and the velocity ratio, and therefore does not affect the surface plot in Fig. 3B of the manuscript.

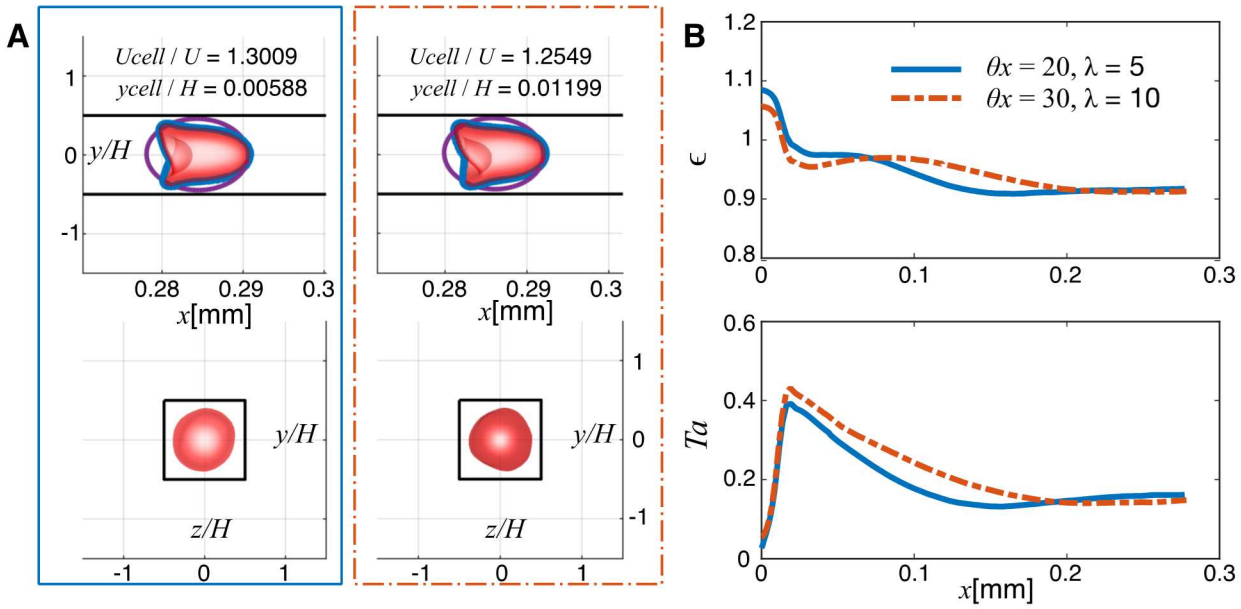

Fig. S5. (A) The final shape of the red blood cells after starting with an angle prior to the entrance of the constriction. The top row shows the shape in the *xy* plane and the bottom row in the *yz* plane. The outline of the cell is shown with blue and the equivalent ellipse is shown with purple. (B) The transient evolution of the confinement level of the cells and the Taylor deformation for two values of the viscosity ratio, 5 (default in our simulations in the main text) and 10.

S.3.2 Impact of κ_b, *Re*, and λ on the steady-state values. As is depicted in Fig. S6 below, we found that increasing the bending ratio, decreasing *Re*, and increasing the viscosity ratio by a factor of two marginally change the steady-state values of the Taylor deformation, confinement, the velocity ratio (maximum of about 3%), and therefore do not affect the surface plot in Fig. 3B. The Re of 0.05-0.1 is consistent with what we have in the experiments and these are all in low-Re regime with the length scale being the channel dimension. In Fig. S6 shown below, we also demonstrate the impact of reducing Re to 0.05, and it is seen that the transient and the steady-state behavior of all critical variables closely follows that of $Re = 0.1$ (default value). In Fig. S6C, we evaluated the impact of higher bending modulus compared to the default value of 0.0033 in our simulations, i.e., $\kappa_b = 0.0066$ for the case of $Ca = 0.4$ and the $\epsilon \approx 1$. While the transient shape evolution is affected by this change in κ_b, the steady-state behavior is marginally affected (negligible impact on the velocity ratio and the Taylor deformation and ~3% for the confinement).

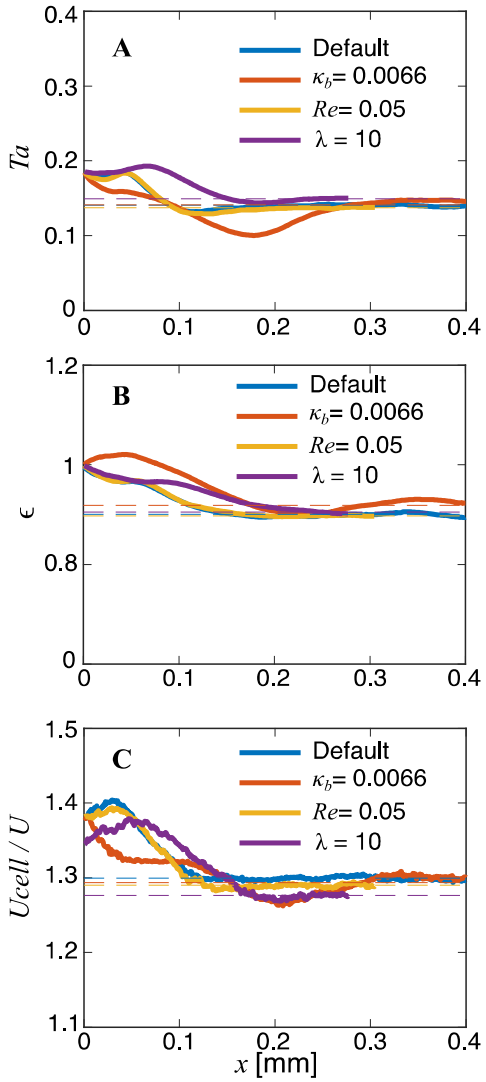

Fig. S6. The sensitivity analysis of the critical variables (A) Taylor deformation Ta, (B) confinement level ϵ, and (C) the velocity ratio for $Ca = 0.4$ and $\epsilon \approx 1$. The dependency of the transient and steady-state behavior of these variables are evaluated for increasing the bending ratio (κ_b), reducing the Re, and increasing the viscosity ratio all by a factor of two compared to the default values taken in our original simulations.

S.4 Experimental setup details

S.4.1 Sample prep. Healthy donor blood samples were obtained with institutional review board approval. Within 30 min of withdrawal, blood was loaded into a lithium heparin tube and centrifuged at 1,200 g and room temperature. Red blood cells (RBCs) were collected and washed twice with phosphate buffered sa1ine solution (Gibco PBS at 1x, pH 7.4, Thermo Fisher, USA) in an Eppendorf tube at 1,200 g for 10 min at room temperature. The RBC pellet was collected and resuspended in fresh PBS to achieve a final hematocrit of 3%. For the stored cell experiments, the RBC pellet was collected and stored in an Eppendorf tube at 4°C for 5 weeks.

S.4.2 Chip fabrication and operation. Microfluidic chips were developed to deform RBCs as they traveled through small, constricted, channel sections. The chip featured an extended serpentine section downstream of the constriction section which increased the hydraulic resistance of the device to enable velocities of order 1 mm s^{-1} for applied inlet gauge pressures of the order 10 kPa. We designed channels of 10 mm length (distance between inlet and outlet), 250 μm width, and 7 μm uniform depth. In the middle region of each channel, we incorporated a constriction of 1 mm length and 7 μm width.

Our devices consisted of a single layer poly-dimethylsiloxane (PDMS) structure bonded to a borosilicate glass cover slip.[24] The cover slip enabled a clear optical path for imaging with an inverted microscope (cf. Section S.4.3). As shown in Fig. S7A, a chrome-on-glass photomask (Front Range Photomask, USA) was fabricated and used for SU-8 lithography on four-inch silicon wafer mold (Microfluidic Foundry, Berkeley, CA, USA). Next, we mixed, degassed, and poured a ratio of 10:1 precursor-to-curing agent of Sylgard 184 (Dow Corning) over our master molds to cast the PDMS structures. The PDMS was allowed to cure in an oven at 55°C for 15 min. We then peeled off the PDMS slab, diced into individual chips (shown in Fig. S7B), and punched 1 mm diameter inlet and outlet holes. Finally, we irreversibly bonded the PDMS structures to number 1 thickness borosilicate glass cover slips by plasma treating both surfaces to be in contact.

To measure an individual's RBC shape morphology distribution, we first dispensed 10-20 μL of the RBC solution as described in S.4.1 into the inlet reservoir of the microfluidic chip. Next, we connected a clear, 1/16" outer diameter poly-tetrafluoroethylene (PTFE) tubing into the same (inlet) reservoir. Finally, as shown in Fig. S7B, we initiated flow of RBCs by applying a positive gauge pressure on the order of 10 kPA at the upstream end of the PTFE tubing. We note that the outlet reservoir was simply held at atmospheric pressure.

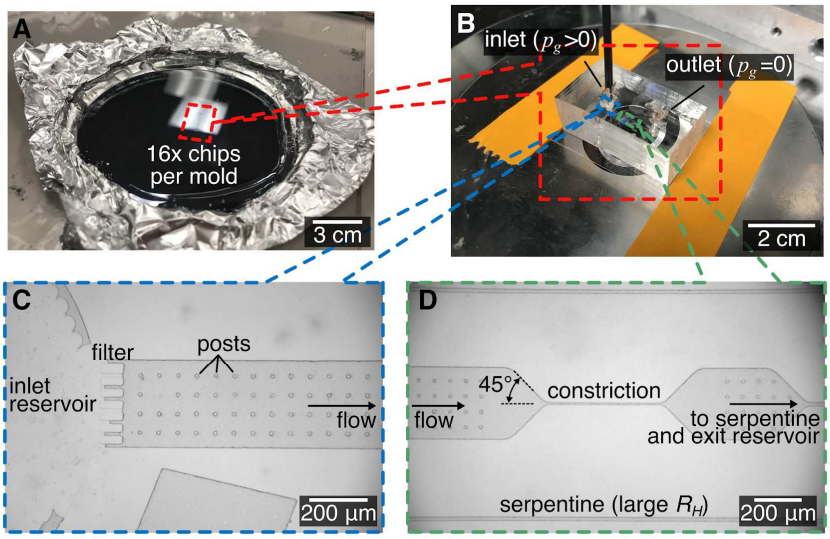

Fig. S7. The cured PDMS slab on top of the SU-8 on four-inch silicon wafer, positive mold is shown in (A). Each mold permitted the fabrication of 16 individual PDMS chips. Individually diced chips were irreversibly bonded to number one thickness glass coverslips, shown in (B), and secured onto the microscope stage using adhesive. After 10-20 μL of an individual's RBC solution was dispensed onto the inlet reservoir, the inlet was pressurized to a gauge pressure on the order of 10 kPa. Panel (C) shows a bright-field image of the microfluidic chip inlet reservoir and 10 μm filter. The posts in the large channel are designed to prevent collapse of the large aspect ratio

channel (1:6). After flowing through the large channel section, RBCs entered the constriction shown in (D). Finally, after cells exit the constriction, they travel through the serpentine channel which is designed with a hydraulic diameter much larger than the rest of the chip. Hence, given a fixed inlet-outlet pressure difference, the resistance of this test section governs the flow rate.

S.4.3 Image acquisition. Fig. S8 shows our experimental setup which includes an inverted microscope (Eclipse TE 300E, Nikon, Japan) and a custom bright field illumination configuration for RBC visualization. A blue, high-power LED (SOLIS-470C, Thorlabs, USA) was first focused into a fiber optic cable using a positive (biconvex) lens, as shown in Fig. S8A. The end of the fiber optic cable, shown in Fig. S8B, was placed above an air immersion 10x/0.30 Olympus objective (Olympus Corporation, Japan) to further condense the LED light as it traveled through the microfluidic chip and the RBCs. The forward elastic scatter was subsequently collected by a water immersion 20x/0.95 Nikon objective (Nikon, Japan), as shown in Fig. S8D. This light was reflected and filtered with a dichroic mirror (XF015-2, Omega Optical, Semrock, USA). Finally, the image was collected by a scientific-grade complementary metal oxide (sCMOS) camera (Hamamatsu ORCA-flash4.0 v2, Hamamatsu Photonics, Japan). The proprietary camera software, HC Image, was used to acquire 16-bit multi-page TIFF files with a region of interest (ROI) of 64 × 2048 pixels (corresponding to 20 × 640 μm in object space). Each multi-page TIFF consisted of 5,000 frames recorded over 20 s.

The high-power LED was operated in pulse width modulation (PWM) mode with a frequency of 250 Hz and a duty cycle of 1% (yielding an LED on-time of 40 μs per pulse). after the camera was externally triggered by a TTL signal from the LED controller and set to a 2 ms integration time. Hence, the camera recorded 250 frames per second with an exposure time of 40 μs. This short exposure time resulted in image streaking of less than 5% of the RBC diameter at the highest velocities of 10 mm s^{-1}. All the experiments shown in this work observed RBC velocities less than 10 mm s^{-1}.

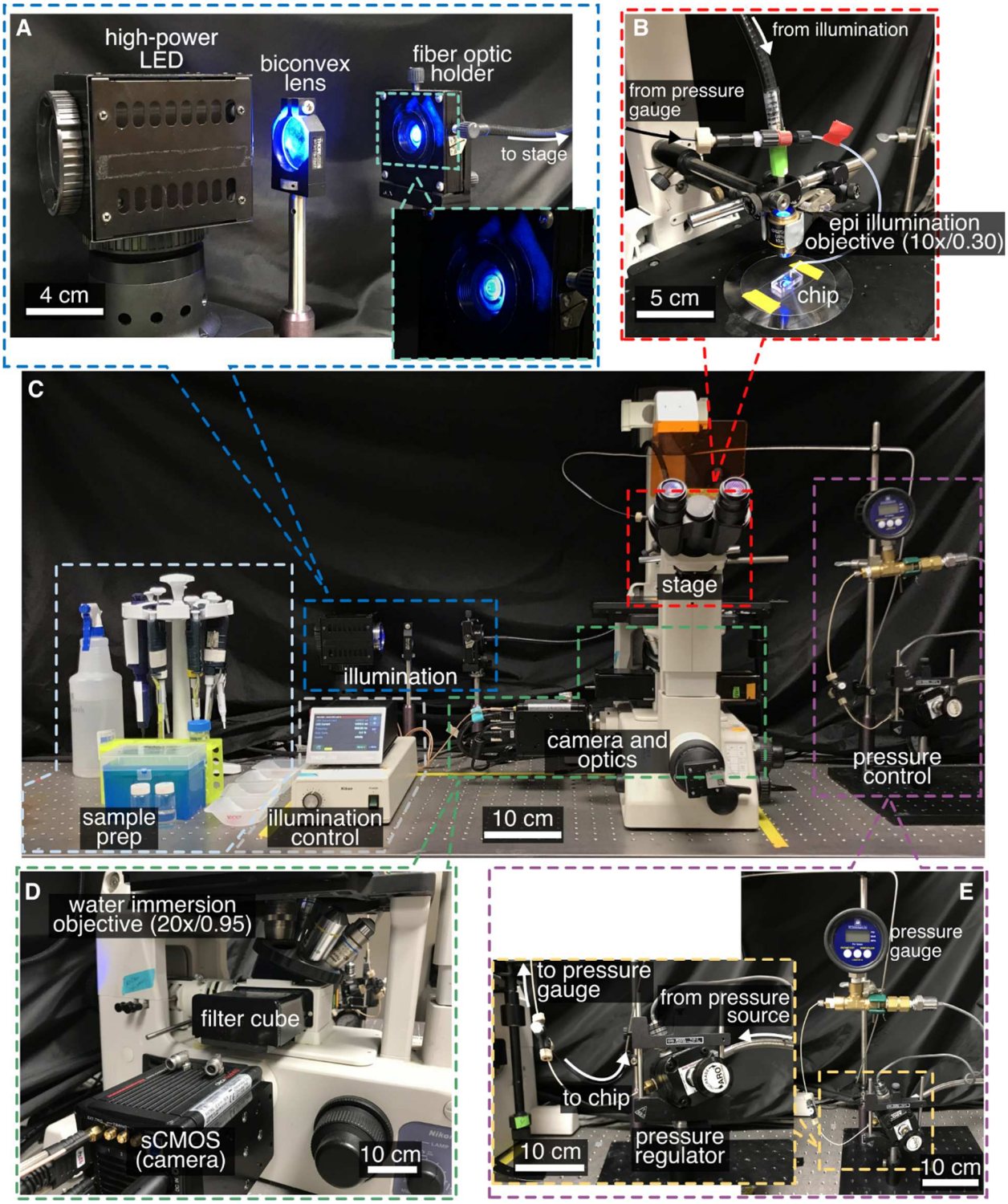

Fig. S8. Experimental setup to record images of an individual's RBCs under shear-induced deformation. The light from a high-power LED was focused into a fiber optic cable (A) and delivered into a 10x/0.30 objective (for further condensation) above the microfluidic chip (B). The overall setup (C) included a water immersion, 20x/0.95 objective for image collection, filter cube, and camera (D). Panel (E) shows the velocity of cells was controlled by adjusting the inlet reservoir pressure.

S.4.4 Images of RBCs in the constriction for different donors. We here show images of RBCs in the entrance region (Fig. S9A) and in the middle of the constriction (Fig. S9B) for the blood from five different healthy donors.

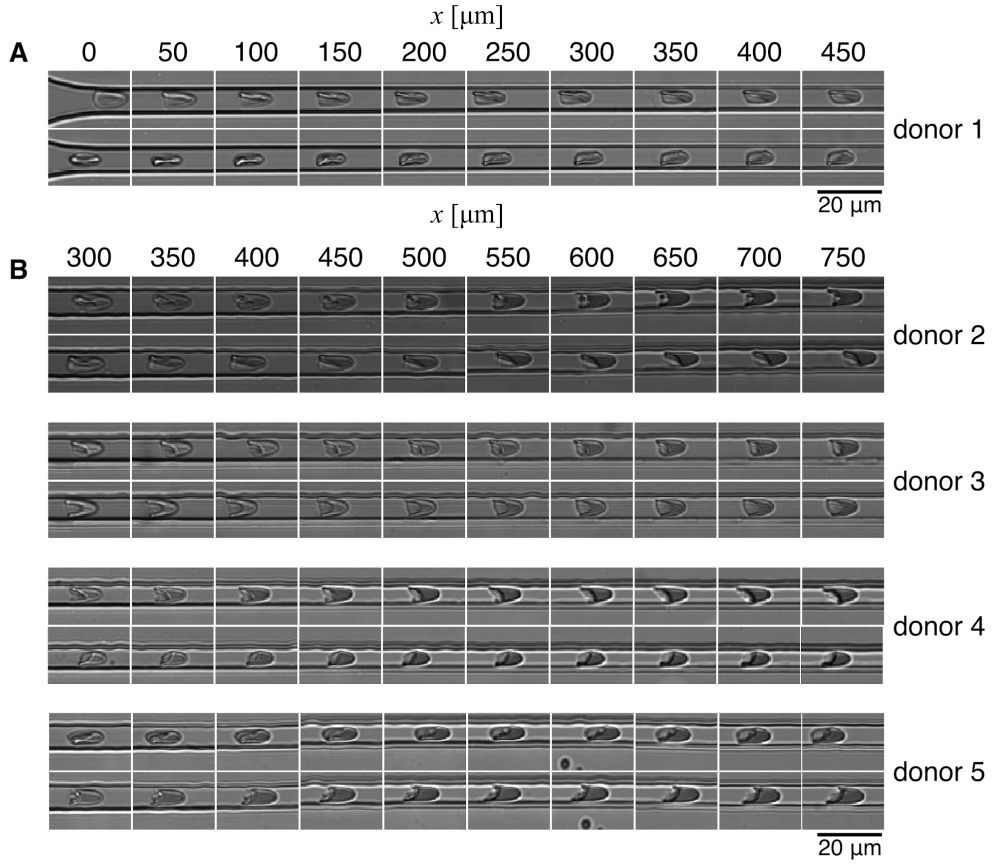

Fig. S9. Example and representative raw (unprocessed) experimental images of RBCs as they enter (A) and reach steady-state shapes (B) within the 7 by 7 μm constriction. Cells were accelerated by applying a small (order 10 kPa) gauge pressure at the microfluidic chip inlet while keeping the outlet at atmospheric pressure. Images were recorded by synchronizing an epi-illumination LED with camera image acquisition. The images above were acquired with effective exposure time of 40 μs at a sampling rate of 250 Hz. Our microfluidic system can record hundreds to thousands of cells in a few seconds. The donors here correspond to the same donors shown in Figs. 4 and 5 of the main text.

S.4.5 Image processing. Prior to cell morphological characterization, raw multi-page TIFF stacks (Fig. S10A) were imported into MATLAB 2019a (Mathworks, USA) and background subtracted (Fig. S10B). The background subtraction was performed by computing the temporal median pixel value at each pixel among ten prior and ten subsequent frames (21 total frames). This "moving median" was subtracted from each pixel. Next, to detect cells, we obtained the absolute value of all frames and performed a multi-step edge detection scheme. This scheme sequentially consisted of: (1) binarization based on background value threshold, (2) area filter to remove objects much larger or smaller than RBC, (3) object dilation to close open edges, (4) flood-fill operation on

holes, and (5) erosion of edges. After computing each cell contour in each frame, the code performed morphological operations and calculations such as area (confinement), *x*-centroid, *y*-centroid, and Taylor deformation parameter, *Ta*, calculation (Fig. S10B). The Taylor deformation was calculated by calculating the cell second area moment, as described in section S.2.2.

Finally, we tracked individual cells across frames by performing a chi-square minimization in which each cell in a frame *i* is matched to a cell in the subsequent frame *i*+1. We chose a chi squared statistic similar to that of Rose et al.[25] which included cell *x*-location (and also adjusted for cell velocity estimate). In our approach, the *x*-coordinate term in the chi-square minimization provided the most efficient discriminant for identifying the same cell across frames. Note cell tracking was robust as the typical distance between cells (shown in Fig. S10C) in a frame was typically larger than the distance travelled by a single cell between adjacent frames. The code can process several 1000's cells in ~10 min.

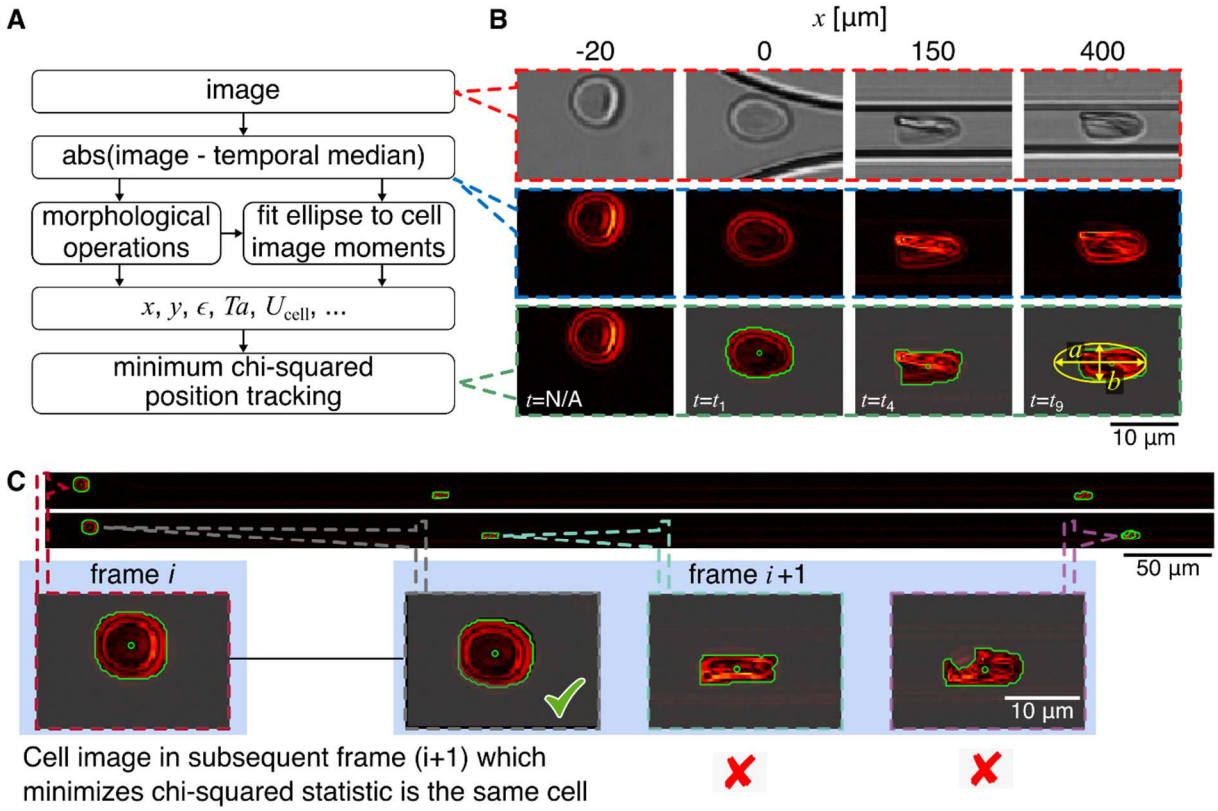

Fig. S10. Summary of automated image processing for cell identification, tracking, and shape quantification. Panel (A) shows a flow chart summarizing morphological processing steps. Panel (B) shows raw (top row), background subtracted and absolute value operation (middle row), and detected cell (bottom row) images. (C) schematically shows the cell tracking component of the image processing code which was implemented in MATLAB. Our code can detect, track, and quantify the shear modulus of thousands of cells in minutes.

S.5 Measurements of shear moduli for many donors

As described in the main text, our platform is capable of quickly obtaining an RBC shear modulus distribution for a donor. Fig. S11 shows the shear modulus distribution of RBCs from six donors

separate from those in the main work. Note that the geometric mean and geometric standard deviation is used, which as mentioned in the main text, is the proper statistical values for a log-normal distribution.

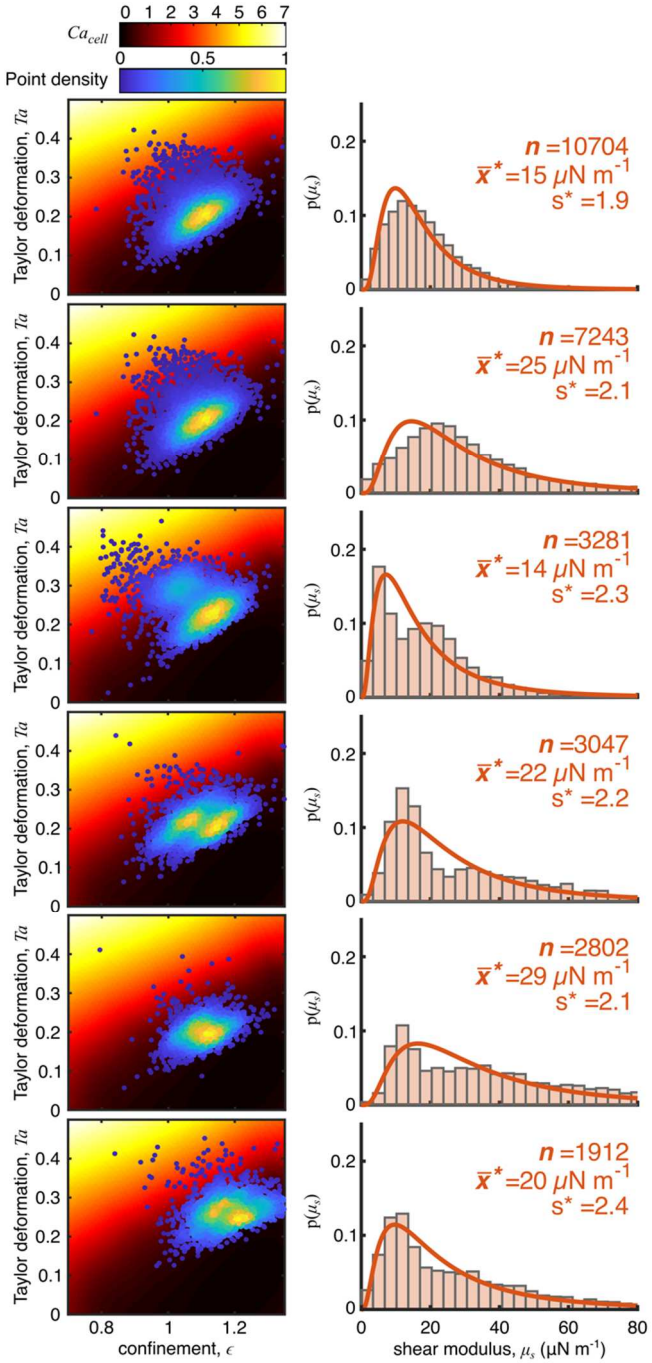

Fig. S11. Plots of Taylor deformation *Ta* versus confinement ϵ data and extracted measurement of shear moduli for six additional donors (each row corresponds to a different donor) beyond those shown in the main work. The dots in the left column shows experimental measurements of the steady values of *Ta* versus ϵ for individual cells. The scattered points are overlaid on the

computationally generated (see Section 2.2 of the main work) Ta versus ϵ surface, where the color at each location corresponds to a cell-specific Capillary number Ca_{cell}. The color of each experimental data point shows the normalized density of points at that location. Ca_{cell}, and the individual cell velocity, are used to predict the shear modulus of a cell. The right column shows probability density functions of shear moduli, generated from the experimental data sets on the right. The six rows correspond to the six individual donor blood samples.

S.6 Comparison of shear moduli with the literature

In Fig. S12, we depict the distribution of the shear modulus taken from all of the healthy donors given in S.4. The corresponding geometric mean and standard deviation is shown in panel B of this figure which is compared with the values of optical tweezers,[26,27] micropipette aspiration,[28,29] and dynamic membrane fluctuation.[30]

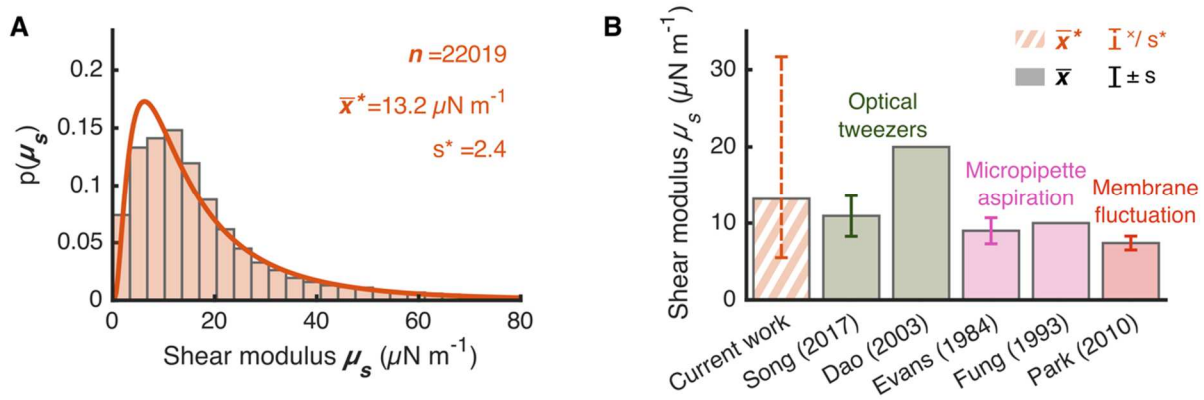

Fig. S12. The comparison of the average shear modulus in our experiment with the ones in the literature. Note that we use a geometric mean $\bar{x}*$ and geometric standard deviation $s*$, since we found that the shear modulus distribution is log-normal. For the literature review, we provide the arithmetic means $\bar{x}$ and standard deviations s.

We can clearly see that the average value of the shear modulus is consistent with standard optical tweezers and micropipette aspiration for normal cells.

S.7 Correlation between shear moduli and cell speed

In addition, we evaluated the correlation of the shear modulus distribution on the velocity of the cells, where we increased the velocity by a factor of 1.5. We found that the shear modulus and its distribution is not correlated with the velocity of the cells.

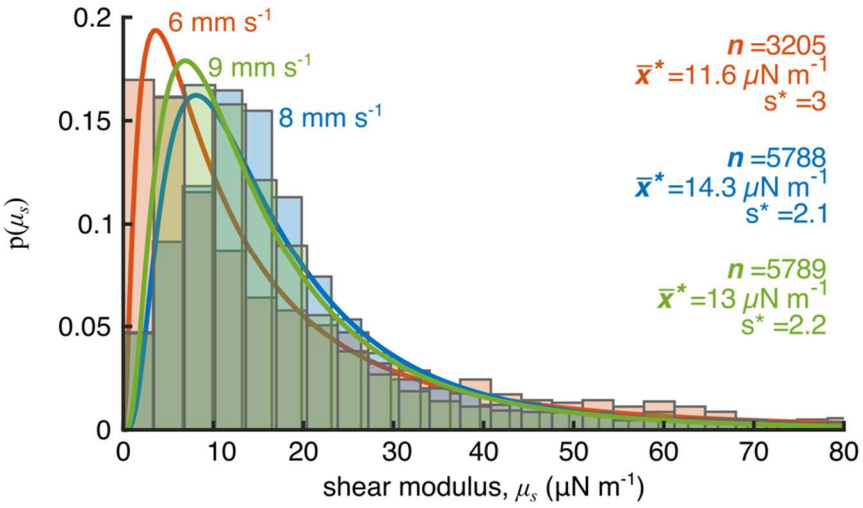

Fig. S13. The shear modulus distribution for three different cell velocities. We expect the shear modulus to not have correlation with the speed of the cells inside the constriction, which is confirmed with this figure.

S.8 Error in experimental measurement of different shape factors

Finally, we here investigated the statistical efficiency of several measures of cell deformation such as Ta, C),[31] (also see SI, S.2.1), eccentricity ε,[32] compactness C_{comp},[33] and [deformation ratio] DR (cf. SI, S.2.3 and related references,[31,34]). We found that image noise has a strong influence on any measure using the length of the contour of the boundary of the cell image. The latter include C and DR. This is apparent from the large image-to-image fluctuation of these quantities for a given cell (c.f. Fig. S14). In contrast, the area moments associated with quantifying Ta are less sensitive to image noise. On the right-hand side of Fig. S14 we show that shape factors determined by second order moments of the cell image (e.g. Ta, ε, and C_{comp}) are more statistically efficient estimators[35] of cell shape and exhibit lower image-to-image variation for the same cell. First, we describe the ε as

$$\varepsilon = \frac{c}{a}, \tag{S17}$$

where c is half of the distance between the foci and a is the major axis length of an ellipse that has the same second order moments as the cell. In turn, C_{comp} is given by

$$C_{comp} = \frac{\sqrt{\frac{4}{\pi}A}}{2a}, \tag{S18}$$

where A is the cell area and $2a$ is (again) the major axis length of an ellipse that has the same second order moments as the cell. Fig. S14 compares these shape factors.

We here describe the formulation of a figure of merit to describe shape factor precision and apply it (Fig. S14) to select the most efficient statistical estimator of deformation. In the

downstream (x > 300 μm) region of the constriction, we expect RBCs to assume a steady state shape. For a single cell, we can make N observations of multiple shape factors $\phi_{i,j}$ (where i and j respectively denote the shape factor and cell number). Note N is the number of frames which capture the cell as it travels across the image ROI and averages around 20 for our experiments. The estimated value of $\phi_{i,j}$ is defined as the cell sample mean $\hat{\phi}_{i,j}$, given by

$$\hat{\phi}_{i,j} = \frac{1}{N}\sum_{k=1}^{N} \phi_{i,j,k}\,, \tag{S19}$$

where k denotes the index of the measurement number for that shape factor. Similarly, the estimated mean shape factor value across all cells $\hat{\phi}_i$, is given by

$$\hat{\phi}_i = \frac{1}{N}\sum_{j=1}^{N} \hat{\phi}_{i,j}, \tag{S20}$$

We hypothesize that, for a fixed shape factor and cell, any variation amongst $\phi_{i,j,k}$ is due to image noise. Hence, the (single-cell) error for each shape factor $\hat{\sigma}_{i,j}$ is here defined as the sample standard deviation of measurements for a single cell. Mathematically,

$$\hat{\sigma}_{i,j} = \sqrt{\frac{1}{N-1}\sum_{k=1}^{N}\left(\phi_{i,j,k} - \hat{\phi}_{i,j}\right)^2}\,. \tag{S21}$$

The absolute value of $\hat{\sigma}_{i,j}$, however, may not be a useful measure of the error associated with the measurement technique. Note there are two sources of variation for each shape parameter: 1) frame to frame error in shape factor measurements for the same cell and 2) underlying distributions of cell mechanical properties which lead to different deformations from cell to cell.

We estimate the underlying variation of a shape factor amongst many cells $\hat{\sigma}_i$ as

$$\hat{\sigma}_i = \sqrt{\frac{1}{N-1}\sum_{j=1}^{N}\left(\hat{\phi}_{i,j} - \hat{\phi}_i\right)^2}\,. \tag{S22}$$

Finally, we quantify the "precision" of a measurement technique as the ratio of the intra-cellular variations of shape factor measurements to the variations among the population. We call this a standard deviation ratio SDR. That is,

$$SDR = \frac{\hat{\sigma}_{i,j}}{\hat{\sigma}_i}. \tag{S23}$$

Note that SDR is evaluated for every shape parameter (index i) and cell (index j).

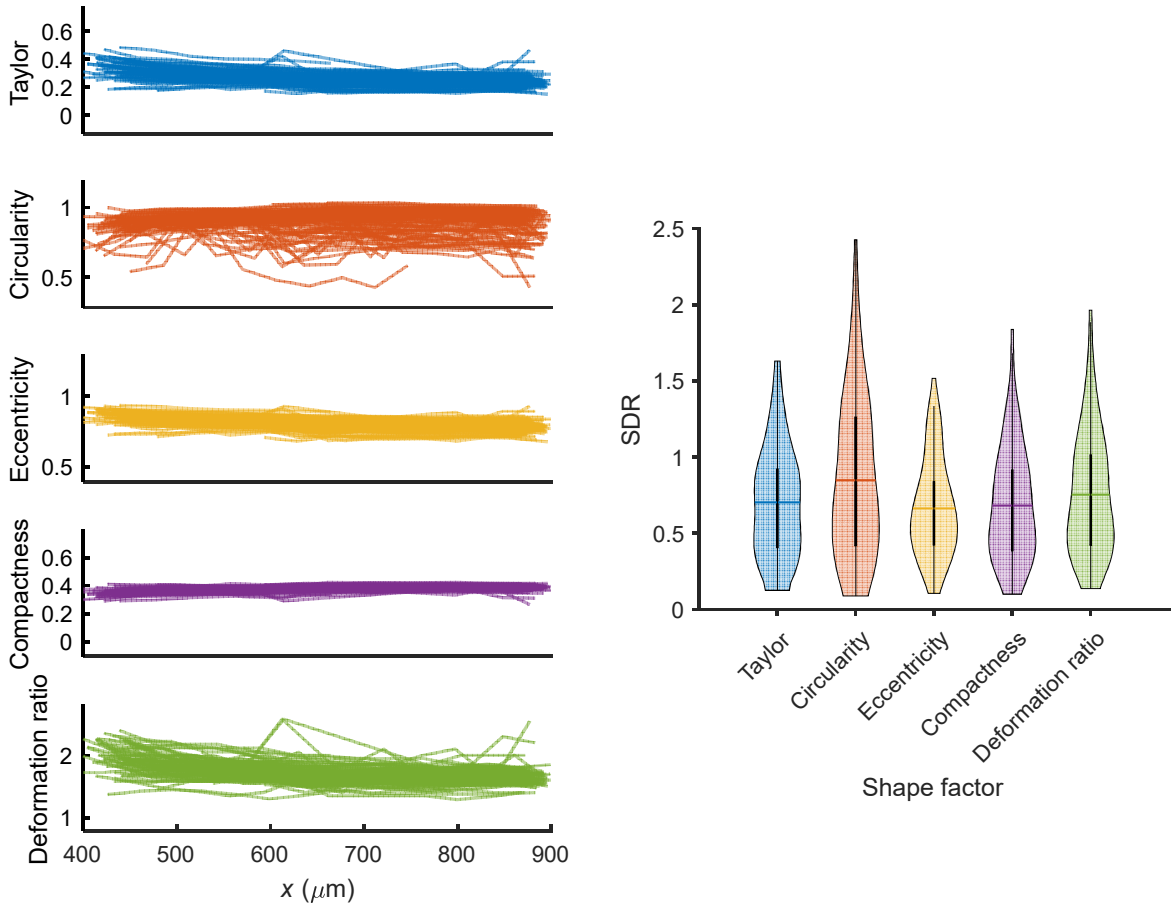

Fig. S14. Quantitative comparison of nondimensional shape factors to measure RBC deformation. On the left are shown (top to bottom) the Taylor deformation Ta, circularity C, eccentricity ε, compactness C_{comp}, and deformation ratio DR versus x for the same group of cells ($n = 100$). Each line represents a single cell trajectory and the lines have been made slightly transparent to convey density information. Since $x > 400$ μm, we expect cells to have achieved a steady state shape. We here define the standard deviation ratio SDR as the ratio of the standard deviation of a shape factor for a single cell trajectory $\hat{\sigma}_{i,j}$ to the standard deviation of mean estimates across all cells $\hat{\sigma}_i$ (i.e. $\sigma_{cell}/\hat{\sigma}_i$). On the right are shown violin plots of the SDR for the same shape factors as on the left. The horizontal lines show the mean SDR of each shape factor. Note that the mean SDRs for Ta, C_{comp}, and ε (which are based on second order moments of the cell image) are smaller than the mean SDRs for C and D (based on zero order moments). This suggests shape factors based on second order moments are more statistically efficient estimators of cell shape and exhibit lower image-to-image variation for the same cell.

S.9 List of supplementary movies

Table S2. Three simulation and two experimental movies are provided and described as follows.

Title	Description

"simulation_shape_evolution.avi"	The simulation result of a single cell with $Ca = 0.8$, started with y-coordinate of about 15 μm, when it is located 20 μm prior to the constriction, and with discoidal orientation of 45 degrees with respect to y-axis.
"simulation_orientation_impact.avi"	The simulation result of two cells with $Ca = 0.4$, started with y-coordinate of 7 μm, when it is located about 15 μm prior to the constriction, and with no discoidal orientation, and with 20 degrees discoidal orientation with respect to y-axis, respectively.
"simulation_location_impact.avi"	The simulation result of four cells with $Ca = 0.4$. The y and z coordinates of the cells are varied to evaluate the impact of initial condition on the final values of Ta and confinement.
"experimental_raw.avi"	Raw experimental images of red blood cells in the middle of the constriction. (The left edge of the frame corresponds to a location 300 μm downstream of the constriction.) The experimental setup is described in Section S.3. The movie has been slowed down 10 times.
"experimental_processed.avi"	Same experimental images as "experimental_raw.avi" with background subtraction, centroid tracking, and edge detection. The process for image processing has been described in Section S.3.5

S.10 References

1 A. Saadat, C. J. Guido, G. Iaccarino and E. S. G. Shaqfeh, *Phys. Rev. E*, 2018, **98**, 063316.

2 R. Skalak, A. Tozeren, R. P. Zarda and S. Chien, *Biophys. J.*, 1973, **13**, 245–264.

3 S. Fitzgibbon, J. Cowman, A. J. Ricco, D. Kenny and E. S. G. Shaqfeh, *Soft Matter*, 2015, **11**, 355–367.

4 K. Sinha and M. D. Graham, *Phys. Rev. E*, 2015, **92**, 042710.

5 Q. M. Qi and E. S. G. Shaqfeh, *Phys. Rev. Fluids*, 2017, **2**, 093102.

6 C. Pozrikidis, *Ann. Biomed. Eng.*, 2003, **31**, 1194–1205.

7 E. Evans and Y.-C. Fung, *Microvasc. Res.*, 1972, **4**, 335–347.

8 D. Cordasco, A. Yazdani and P. Bagchi, *Phys. Fluids*, 2014, **26**, 41902.

9 Z. Peng, A. Mashayekh and Q. Zhu, *J. Fluid Mech.*, 2014, **742**, 96–118.

10 S. K. Doddi and P. Bagchi, *Phys. Rev. E*, 2009, **79**, 46318.

11 S. Krishnan, E. S. G. Shaqfeh and G. Iaccarino, *J. Comput. Phys.*, 2017, **338**, 313–338.

12 J. B. Freund, *Annu. Rev. Fluid Mech.*, 2014, **46**, 67–95.

13 D. A. Fedosov, B. Caswell, A. S. Popel and G. E. Karniadakis, *Microcirculation*, 2010, **17**, 615–628.

14 R. M. Hochmuth, P. R. Worthy and E. A. Evans, *Biophys. J.*, 1979, **26**, 101–114.

15 P. Cicuta, S. L. Keller and S. L. Veatch, *J. Phys. Chem. B*, 2007, **111**, 3328–3331.

16 B. B. Chaudhuri and G. P. Samanta, *Pattern Recognit. Lett.*, 1991, **12**, 1–7.

17 L. Rocha, L. Velho and P. C. P. Carvalho, in *Proceedings. XV Brazilian Symposium on Computer Graphics and Image Processing*, IEEE Comput. Soc, 2002, pp. 99–105.

18 L. L. Wheeless, R. D. Robinson, O. P. Lapets, C. Cox, A. Rubio, M. Weintraub and L. J. Benjamin, *Cytometry*, 1994, **17**, 159–166.

19 O. Otto, P. Rosendahl, A. Mietke, S. Golfier, C. Herold, D. Klaue, S. Girardo, S. Pagliara, A. Ekpenyong, A. Jacobi, M. Wobus, N. Töpfner, U. F. Keyser, J. Mansfeld, E. Fischer-Friedrich and J. Guck, *Nat. Methods*, 2015, **12**, 199–202.

20 K. Khairy and J. Howard, *Med. Image Anal.*, 2008, **12**, 217–227.

21 R. Wells and H. Schmid-Schönbein, *J. Appl. Physiol.*, 1969, **27**, 213–217.

22 L. Lanotte, J. Mauer, S. Mendez, D. A. Fedosov, J.-M. Fromental, V. Claveria, F. Nicoud, G. Gompper and M. Abkarian, *Proc. Natl. Acad. Sci.*, 2016, **113**, 13289–13294.

23 T. W. Secomb, *Annu. Rev. Fluid Mech.*, 2017, **49**, 443–461.

24 D. C. Duffy, J. C. McDonald, O. J. A. Schueller and G. M. Whitesides, *Anal. Chem.*, 1998, **70**, 4974–4984.

25 K. A. Rose, J. A. Meier, G. M. Dougherty and J. G. Santiago, *Phys. Rev. E*, 2007, **75**, 11503.

26 H. Song, Y. Liu, B. Zhang, K. Tian, P. Zhu, H. Lu and Q. Tang, *Biomed. Opt. Express*, 2017, **8**, 384.

27 M. Dao, C. T. Lim and S. Suresh, *J. Mech. Phys. Solids*, 2003, **51**, 2259–2280.

28 E. Evans, N. Mohandas and A. Leung, *J. Clin. Invest.*, 1984, **73**, 477–488.

29 Y.-C. Fung, *Biomechanics: Mechanical Properties of Living Tissues*, Springer, 1993.

30 Y. K. Park, C. A. Best, K. Badizadegan, R. R. Dasari, M. S. Feld, T. Kuriabova, M. L. Henle, A. J. Levine and G. Popescu, *Proc. Natl. Acad. Sci. U. S. A.*, 2010, **107**, 6731–6736.

31 M. Urbanska, H. E. Muñoz, J. Shaw Bagnall, O. Otto, S. R. Manalis, D. Di Carlo and J. Guck, *Nat. Methods*, 2020, 1–7.

32 C. Fatichah, D. Purwitasari, V. Hariadi and F. Effendy, *Int. J. Smart Sens. Intell. Syst.*, 2014, **7**, 1271–1286.

33 P. Ruusuvuori, A. Lehmussola, J. Selinummi, T. Rajala, H. Huttunen and O. Yli-Harja, *Eur. Signal Process. Conf.*

34 J. C. A. Cluitmans, V. Chokkalingam, A. M. Janssen, R. Brock, W. T. S. Huck and G. J. C. G. M. Bosman, *Biomed Res. Int.*, 2014, **2014**, 1–9.

35 J. S. Bendat and A. G. Piersol, *J. Am. Stat. Assoc.*, 1987, **82**, 1197.